



Technical note: Disentangling pre- and post-depositional thermal histories in partially reset samples

Birk P. Härtel, Eva Enkelmann, and Akeek Maitra

Department of Earth, Energy, and Environment, University of Calgary, Calgary, AB, T2N 1N4, Canada

5 *Correspondence to:* Birk Härtel (birk.haertel@ucalgary.ca)

Abstract. Interpreting thermochronological data of a partially reset detrital sample is challenging because its age distribution reflects a mixture of each grain's individual pre-depositional and the shared post-depositional thermal history. A promising approach to meet this challenge is combined geo- and thermochronological dating on the same grains. We present an algorithm for disentangling the pre- and post-depositional thermal histories using data from zircon U/Pb-(U-Th)/He double-
10 dating. It proceeds in three steps: (1) determining candidate post-depositional temperature-time paths by inverse thermal-history modeling of syn-depositional grains. (2) Calculating pre-depositional (U-Th)/He model ages for each candidate thermal history. (3) Evaluating the likelihood for each post-depositional history by testing if resulting pre-depositional model ages against the U-Pb crystallization ages of each grain and the timing of sediment deposition. We illustrate this strategy by applying it to a Devonian sandstone from the Northern Canadian Cordillera. The results show the general agreement of the
15 modeled thermal histories and pre-depositional (U-Th)/He ages with existing thermochronological data. The temperature-time paths are also consistent with additional zircon-Raman thermochronological data from the same grains. We discuss the limitations of our approach imposed by the need for syn-depositional grains, its application to other thermochronometers, and how targeting rather than avoiding partially reset samples enhances our capability to extract thermal-history information from the detrital record.

20 **1 Introduction**

Detrital thermochronology is a powerful tool to date thermal events in sediment basins and their source regions (e.g., Garver et al., 1999; Malusà and Fitzgerald, 2020). The information we obtain from detrital thermochronology depends on the sample's post-depositional history as shown in Fig. 1: an unreset sample (blue line in Fig. 1a) stayed at temperatures lower than the partial retention zone (PRZ). Its grains did not lose radioactive-decay products (daughters) during post-depositional
25 heating. Its single-grain ages thus pre-date deposition (Fig. 1b); their variation mainly reflects different pre-depositional thermal histories and provides valuable information about cooling of the sources (e.g., Garver et al., 1999; Rahl et al., 2003; Enkelmann et al., 2008; Bernet and Garver, 2005; Malusà and Fitzgerald, 2020). A fully reset sample was reheated well above the PRZ, erasing prior age information (yellow line in Fig. 1a). Its single-grain age distribution displays one age peak post-dating deposition (Fig. 1b). Minor, within-sample age differences occur due to thermal-sensitivity differences between



30 grains, e.g., related to properties such as grain size, composition, or radiation damage (Carlson et al., 1999; Reiners and Farley, 2001; Flowers et al., 2009; Guenther et al., 2013). Reset samples allow us to constrain the time of post-depositional cooling in the basin (e.g., Cecil et al., 2014, Enkelmann et al., 2014; McKay et al., 2021).

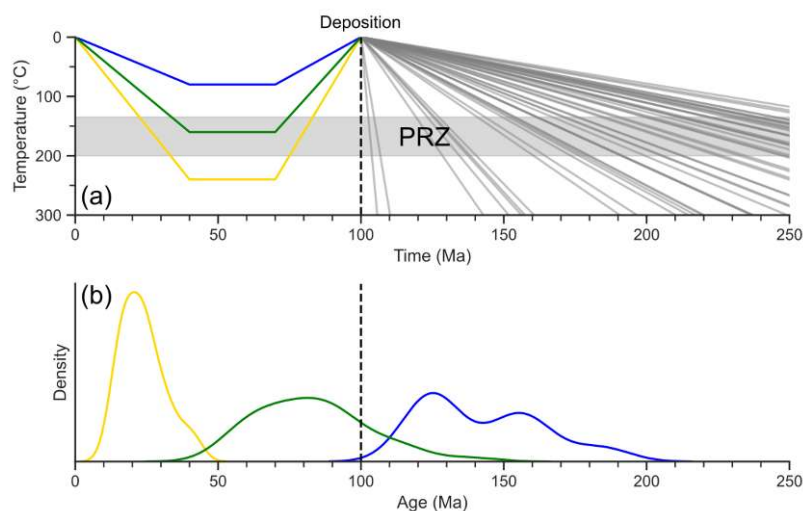


Figure 1: Schematic thermal histories and single-grain age distributions of unreset (blue), partially reset (green), and fully reset (yellow) sedimentary samples in the zircon (U-Th)/He (ZHe) system. (a) Example thermal histories for detrital grains with individual pre-depositional (grey) temperature-time (T-t) paths and shared post-depositional paths. The grey shaded area marks the partial retention zone (PRZ; kinetics of Reiners et al., 2004, for non-metamict zircon grains with equivalent spherical radii of 20–90 μm and 30 Myr holding time). (b) Kernel-density estimate (KDE) curves for synthetic age distributions reflecting the thermal histories in (a).

In contrast, a partially reset sample experienced post-depositional heating into the PRZ (green line in Fig. 1a). It retained only part of its accumulated daughters after deposition and the age distribution spans across the depositional age (Fig. 1b).
35 The single-grain ages vary due to both, differences in pre-depositional thermal histories and differences between the thermal sensitivity of individual grains. With increasing degree of partial reset, the age spectrum approaches that of a fully reset sample. For very low or high degrees of partial reset, within-sample thermal-sensitivity differences even enable the co-existence of partially reset grains with unreset or fully reset grains.

In theory, partially reset samples hold information on both the pre- and post-depositional history that is inaccessible for fully
40 reset or unreset samples: on one hand, the mere notion of a sample having spent time within the well-defined temperature window of the PRZ provides a more precise estimate on the timing and temperature of maximum heating rather than just an upper (unreset) or lower (fully reset) temperature limit. On the other hand, correcting the observed thermochronological ages



for post-depositional heating would allow to extract the time when the source rocks cooled (e.g., Reiners et al., 2005) –
45 information beyond the reach of fully reset samples.

However, accurate interpretation of thermochronological data from partially reset detrital samples is complicated by the
single-grain ages representing a mixture of the shared post-depositional and the individual pre-depositional thermal histories
(Reiners et al., 2005; Flowers et al., 2022). The most promising approach for disentangling pre- and post-depositional
thermal histories is combined thermochronological and geochronological dating of the same grains (e.g., Carter and Moss,
50 1999; Reiners et al., 2005; Enkelmann et al., 2019a; Bootes et al., 2019; Danišik, 2019; Dunkl et al., 2024). In the popular
zircon U/Pb–(U-Th)/He double-dating scheme, the U/Pb ages – commonly interpreted as crystallization ages – provide
individual constraints on the start of the thermal history for each grain that can be used for forward and inverse thermal-
history models of each grain (Reiners et al., 2005; Fosdick et al., 2015; Yonkee et al., 2019). Nevertheless, the existing
interpretation strategies for partially reset samples based on double-dating rely on assumptions about the pre-depositional
55 thermal history. That knowledge is often not available, especially for pre-Cenozoic sediments because the specific sources
have been eroded. An alternative approach is therefore necessary, particularly in the light of the in-situ ZHe-U/Pb double-
dating technique by laser ablation, which allows acquiring large numbers of detrital-zircon double-dates (e.g., Vermeesch et
al., 2012; Tripathy-Lang et al., 2013; Evans et al., 2015; Forte et al., 2022; Zawacki et al., 2024; Dunkl et al., 2024).

Building on the approaches of Reiners et al. (2005) and Fosdick et al. (2015), we present a new interpretation strategy for
60 combined ZHe and U/Pb data from partially reset samples. It avoids assumptions on the pre-depositional history by relying
on syn-depositional grains. Our approach proceeds in three steps: (1) finding candidate temperature-time (T-t) paths for the
post-depositional history by inverse T-t modeling of syn-depositional grains; (2) calculating pre-depositional model ages for
each grain and each candidate T-t path; (3) evaluating the plausibility of post-depositional thermal histories based on the fit
of the pre-depositional model ages to the constraints imposed by the individual crystallization ages and the depositional age.
65 We first explain the details of our new approach in comparison to existing interpretation strategies and apply it to a partially
reset Devonian sandstone from the Northern Canadian Cordillera. The results show that our strategy allows extraction of
meaningful information on the pre- and post-depositional histories from ancient sediments. We then discuss (1) the limits of
our method, including the requirement of syn-depositional grains, problems with nearly fully-reset samples, and simplifying
assumptions in He-diffusion modeling, (2) the application of our modeling strategy to other double-dating schemes, and (3)
70 the question if it is necessary to model partially reset samples. Alongside this publication we provide *PaRACAS* (*Partial
Reset Analysis for Cooling Ages of Sources*), a jupyter notebook that provides the functions for determining pre-depositional
ages from double-dating results and post-depositional histories (Härtel, 2026).

2 Interpretation strategies for partially reset samples using combined zircon U/Pb–(U-Th)/He dating

While it is clear when fully reset or unreset samples accumulated the bulk of their daughters, partially reset samples contain
75 a mixture of pre- and post-depositional daughters. Interpreting partially reset zircon (U-Th)/He (ZHe) data with standard



inverse thermal-history modeling (e.g. Ketcham, 2005, 2024; Gallagher, 2012) starting at the depositional age suffers from two biases. On one hand, for samples with many ZHe ages pre-dating deposition, the models underestimate post-depositional temperature: to reach a good fit with the measured ages all T-t paths need to ensure accumulation and retention of enough He in a restricted time frame. On the other hand, if most ZHe ages post-date deposition, matching the T-t paths with the measured data leads to overestimation of post-depositional temperature toward a full-reset scenario. A widely-used approach is forward-modeling the thermal history with an ‘inheritance envelope’ of pre-depositional residence near the surface or a pre-depositional cooling rate (e.g., Fillon et al., 2013; Cecil et al., 2014; Guenther et al., 2015; Powell et al., 2016, 2020; Fox et al., 2019; Yonkee et al., 2019). Its main advantage is that it allows accumulating not only pre-depositional He but also radiation damage that affects the thermal sensitivity of the ZHe system (Hurley et al., 1956; Reiners et al., 2005; Guenther et al., 2013). This approach evaluates the model fit by comparing the predicted relationship between ages and effective uranium concentrations (eU) to the measured data. However, this approach requires at least endmember assumptions about the pre-depositional thermal history, which is usually unknown and varies from grain to grain.

Combining ZHe and U/Pb dating on the same detrital grains imposes constraints on the pre- and post-depositional histories, as the U/Pb of each grain marks the starting point of its thermal history. For example, the observed amount of He loss since crystallization is a proxy for the degree of reset (Reiners et al., 2005), and each grain’s U/Pb age is a high-temperature starting point for thermal-history modeling (Fosdick et al., 2015). Figure 2 illustrates three interpretation strategies on a synthetic U/Pb–ZHe dataset (Supplement Table T1; $n = 10$) with U/Pb ages ranging from 50 to 205 Ma, with grain sizes (equivalent spherical radii) between 36 and 122 μm . The grains underwent different thermal histories before deposition at 45 Ma (Fig. 2a; crosses: true pre-depositional ZHe ages) and were heated together to a maximum temperature of 168 $^{\circ}\text{C}$ at 25 Ma (thermal-history data in Supplement Table T2). The resulting ZHe ages (31 to 124 Ma) span across the depositional age (dashed line) and correlate positively with the U/Pb ages (Fig. 2b). This relationship reflects the ZHe-age variation due to different pre-depositional thermal histories.

Reiners et al. (2005) present a first-order interpretation approach to estimate the maximum-heating temperature for a simple post-depositional thermal history and a correction approach to obtain ZHe ages of pre-depositional cooling (Figs. 2c–e). Their first step is forward-modeling the ZHe ages for a set of post-depositional thermal histories (Fig. 2c) assuming that every grain stayed at surface temperatures between crystallization and deposition (solid grey line). Figure 2d plots the modeled ZHe ages against the U/Pb ages with fields for each maximum temperature and the measured grain-size range. The further interpretation relies on the fraction of total He loss f_{total} :

$$f_{total} = 1 - \frac{t_{ZHe} - t_{reset}}{t_{UPb} - t_{reset}} \quad (1),$$

where t_{ZHe} and t_{UPb} are the ZHe and U/Pb ages, respectively, and t_{reset} is the time of post-depositional resetting (here: 25 Ma). The grain closest to the equal-age line (solid black line) lost the least He since crystallization ($f_{total} = f_{min}$). f_{min} denotes the maximum possible He loss that can have occurred to all grains together after deposition, indicating the maximum post-



depositional temperature. The grain with the lowest total He loss in Fig. 2d (arrow) suggest that heating reached between 160 and 180 °C, an interval containing the true maximum temperature of 168 °C.

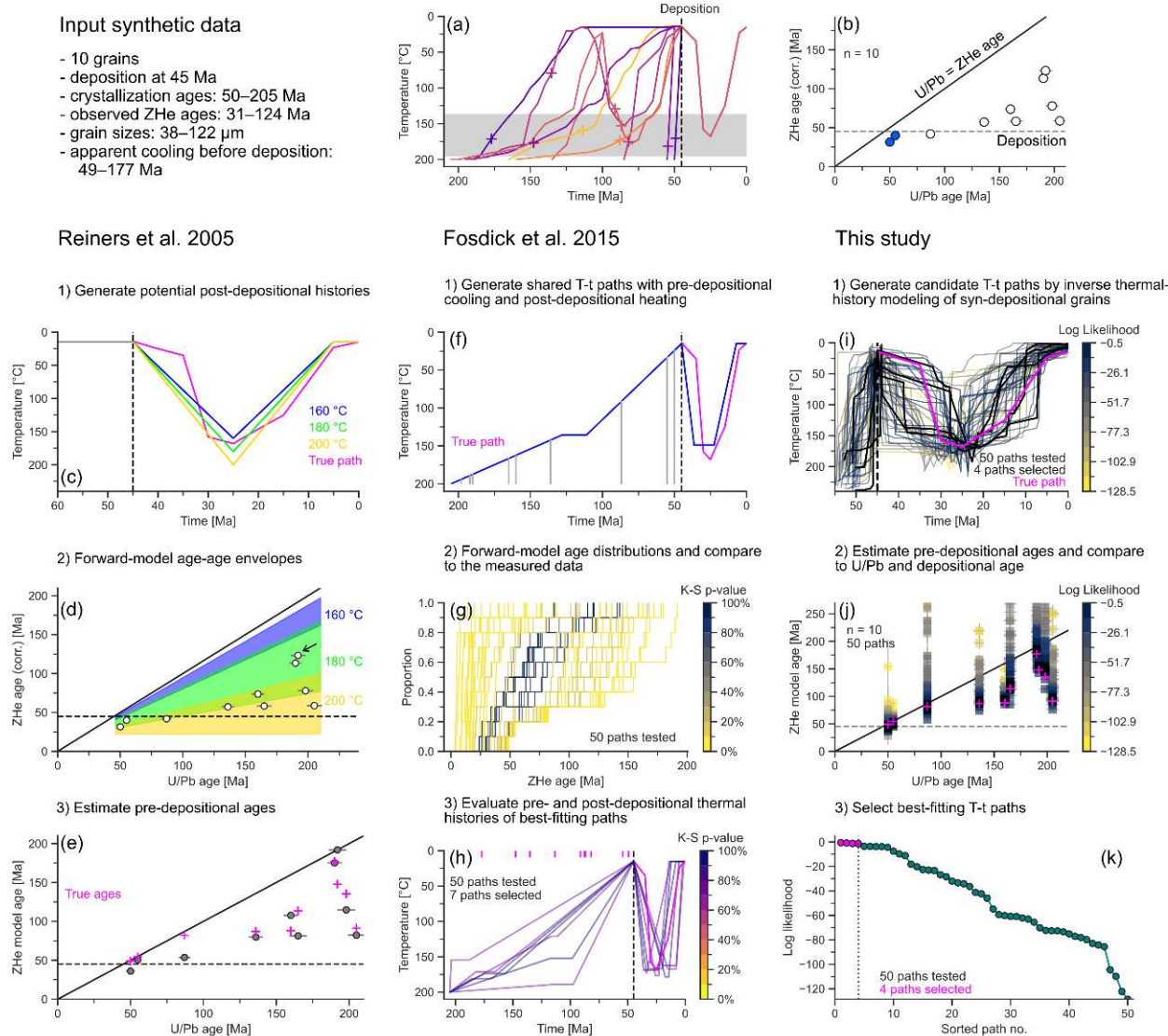


Figure 2: Overview of partial-reset-modeling strategies applied to a synthetic zircon U/Pb–(U-Th)/He dataset. All information on this dataset is provided at the top panel. (a) True temperature-time (T-t) paths for each grain. The grey-shaded area marks the zircon (U-Th)/He (ZHe) partial retention zone (grain size of the synthetic grains; kinetic parameters of Reiners et al., 2004) and (b) ZHe-U/Pb age-age plot. The panels below show the three different interpretation strategies of Reiners et al. (2005; c–e), Fosdick et al. (2015; f–h) and this study (i–k), each in three analytical steps. Detailed description of the specific steps for each strategy in the text.



110 f_{min} also allows correcting all ZHe ages for the maximum possible post-depositional He loss and determining a pre-depositional model ZHe age t_{model} .

$$t_{model} = t_{reset} + \frac{t_{ZHe} - t_{reset}}{1 - f_{min}} \quad (2).$$

Figure 2e plots these model ages against the U/Pb ages (grey circles) and compares them to the ‘true’ pre-depositional ages calculated from forward-modelling the paths in Fig. 2a up to the depositional age (pink crosses).

115 While the pre-depositional ages are a first approximation, six out of ten grains deviate from the true pre-depositional ages by more than 10 Myr – one model age even post-dates the timing of deposition (dashed line). This discrepancy results from extrapolating the annealing kinetics of the least-reset grain to the other grains. If the least-reset grain is more retentive than the average grain, eq. (2) under-corrects the ages (Fig. 2e). Reiners et al. (2005) discuss two additional limitations: first, the model assumes that the grains cooled rapidly after crystallization and stayed near the surface until deposition. This neglects
120 pre-depositional residence in the PRZ. f_{min} is thus a maximum estimate of the post-depositional reset of the least-reset grain and the model age may still overestimate the pre-depositional age. This is particularly a problem for samples with many grains post-dating deposition. Second, depending on the relationship between the depositional age and the measured ZHe ages, the assumed value of t_{reset} may have a strong impact on the pre-depositional ages. Nevertheless, this interpretation approach is a simple method for narrowing down the maximum post-depositional temperature. It is also independent of a
125 specific He-diffusion model, as long as the diffusion kinetics are sufficiently similar across grains.

In contrast, Fosdick et al. (2015) present an approach that models combined pre- and post-depositional thermal histories. It uses forward-modeling of T-t paths characterized by a post-depositional heating pulse (blue path, Fig. 2f) and a pre-depositional cooling history, to which every grain rapidly cooled immediately after crystallization (Fig. 2f). Fosdick et al. (2015) generate a large set of T-t paths with different maximum temperatures, timings and durations of residence in the PRZ
130 and model the present-day single-grain ZHe ages for each path. They evaluate the modeled and observed ZHe age distributions with a two-sample Kolmogorov-Smirnov (K-S) test (cumulative-distribution plot in Fig. 2g), keeping only the best-fitting paths for model interpretation (K-S p-value >68 %; blue and black lines). Finally, they compare the pre- and post-depositional histories of these best-fitting models (Fig. 2h). For our synthetic data, the seven best-fitting T-t paths cluster at maximum temperatures of 160 to 180 °C, which they reached between 40 and 15 Ma and held for 2–13 Myr. Their timing
135 and maximum temperature of post-depositional heating agrees to a first degree with the input thermal history (pink line). The time of pre-depositional cooling through the PRZ for these models spans a large range from 200 to about 100 Ma containing most of the true pre-depositional ages (pink vertical ticks).

One of this method’s drawbacks is that it does not evaluate pre-depositional cooling on a grain-by-grain basis, but only for the bulk sample. Thus, sources with different cooling histories contributing only few grains to the sample will be overlooked
140 because the best-fitting paths are selected based on the bulk goodness-of-fit. Nevertheless, this approach is more flexible than that of Reiners et al. (2005) for testing different pre- and post-depositional histories and considers kinetic differences between grains.



The main limitation for both of these modeling approaches is that both assume either a specific pre-depositional history or at least uniform pre-depositional histories for every grain. We therefore present an alternative modeling strategy (Fig. 2i-k) that avoids this assumption relying on two fundamental principles: (1) syn-depositional grains in a sample record only the post-depositional thermal history (see discussion in Fosdick et al., 2015), and (2) cooling through the PRZ in the source areas happened after crystallization but before deposition. Our strategy combines the probabilistic evaluation of T-t paths of Fosdick et al. (2015) and the pre-depositional model ages of Reiners et al. (2005). Its first step consists in identifying syn-depositional or near syn-depositional grains based on the U/Pb and the depositional ages (blue circles in Fig. 2b). We use these grains for inverse thermal-history modeling in HeFTy (Ketcham, 2005; 2024) to obtain candidate post-depositional T-t paths (Fig. 2i). In the second step, we evaluate each of these paths by calculating pre-depositional model ages. To this end, we determine the net amount of helium accumulated after deposition, He_{post} , and the remaining fraction ϕ_{post} of pre-depositional He by forward-modeling the candidate post-depositional T-t paths (details in Appendix A). Analogous to eq. (2), we calculate the pre-depositional He concentration He_{pre} from the present-day concentration He_{obs} , He_{post} and ϕ_{post} .

$$He_{pre} = \frac{(He_{obs} - He_{post})}{\phi_{post}} + He_{post} \quad (3).$$

The pre-depositional ZHe model age then follows from a generic age equation (Härtel and Enkelmann, 2024) and adding the depositional age t_{dep} for scaling:

$$t_{model} = \frac{1}{\lambda_{238}} \ln \left(1 + \frac{He_{pre} M_{238}}{eU_{pre} 8} \right) + t_{dep} \quad (4).$$

M_{238} , λ_{238} , and 8 are the molar mass of ^{238}U , its decay constant, and the number of α -disintegrations in its decay chain, respectively. eU_{pre} is the pre-depositional effective uranium concentration, i.e., the concentrations of U and Th at the timing of deposition recalculated to the integrated decay rate of ^{238}U between t_{model} and t_{dep} .

We evaluate each path based on the log-likelihood of the pre-depositional model ages falling into the expected envelopes between the individual U/Pb ages and the depositional age (details in Appendix B). Figure 2j plots the model ages against the U/Pb ages, color-coded by their likelihood. Each vertical string of squares represents the set of model ages of one grain for the different T-t paths. The higher-log-likelihood paths (blue and black squares) mostly fall between the equal-age (solid) and depositional-age (dashed) lines. Based on this likelihood, we apply a ‘knee-detection’ algorithm to determine a cutoff likelihood for selecting a set of best-fitting paths (dotted line in Fig. 2k; Satopää et al., 2011). For the synthetic dataset, the algorithm suggests four thermal histories (pink circles). Their post-depositional T-t paths (thick black lines in Fig. 2i) reach maximum temperatures of 160 to 190 °C between 25 and 20 Ma, close to the true thermal history (pink line). These best-fitting T-t paths also predict pre-depositional ages (black squares in Fig. 2j) matching the true pre-depositional ages within 10 Myr (pink crosses). Building on the strategy of Fosdick et al. (2015) to evaluate a large range of possible T-t paths, our strategy uses Monte-Carlo-based inverse thermal-history modeling to address complex post-depositional thermal histories that would be tedious to implement in pure forward-modeling approaches. On the other hand, it preserves the grain-by-grain



175 calculation of pre-depositional model ages of Reiners et al. (2005) that allows comparing different age populations in terms of other single-grain provenance data such as grain size, mineral chemistry, or ϵ_{Hf} values (e.g. von Eynatten and Dunkl, 2012; Sundell and Saylor, 2021). The good fit of our models to the synthetic dataset confirms the validity this approach in theory. In the following section, we illustrate its use on actual thermochronological data from the Northern Canadian Cordillera.

3 Example: zircon U/Pb–(U-Th)/He–Raman data from a Devonian sandstone, Northern Canadian Cordillera

180 We applied our new modeling strategy to zircon U/Pb-(U-Th)/He-Raman multi-chronometer data from a Devonian sandstone (Imperial Formation) from the Mackenzie Plain, Northern Canadian Cordillera. The data were acquired in three steps: Raman spectroscopic radiation-damage mapping of the ν_3 and external rotation (ER, 356 cm^{-1}) bands, He extraction from a small volume within the grains by laser-ablation noble-gas mass spectrometry (e.g., Boyce et al., 2006; Vermeesch et al., 2012; Evans et al., 2015), and LA-ICP-MS for determining the U and Th concentrations – to calculate the ZHe and
185 zircon Raman ages – and the U/Pb age. For details on the analytical procedure and data treatment, see Härtel et al. (2026; their sample NW-15). Figure 3a shows the combined ZHe and concordant zircon U/Pb data. U/Pb ages range from 364 Ma to 2.9 Ga. ZHe ages span a range between 57 and 2030 Ma, across the depositional age of $364.3 \pm 5.7 \text{ Ma}$ (dashed line in Fig. 3a; maximum-depositional age of Härtel et al., 2026); about 73 % of the grains post-date the depositional age. The ZHe ages also show a weak positive correlation with the U/Pb ages. These observations confirm a high degree of partial reset by
190 heating into the ZHe PRZ after deposition as suggested by thermal-history models on other Imperial-Formation samples from Northern Canada (Issler et al., 2005; Enkelmann et al., 2019b; Powell et al., 2020; Spalding et al., 2023).

For the inverse thermal-history modeling, we selected the three youngest grains with concordant U/Pb ages $< 400 \text{ Ma}$ (uncorrected ZHe ages: $106.1 \pm 20.1 \text{ Ma}$ (2s); $157.5 \pm 25.7 \text{ Ma}$; $266.7 \pm 40.3 \text{ Ma}$; blue circles in Fig. 3a), allowing for individual pre-depositional thermal histories of $\leq 36 \text{ Myr}$, less than 10 % of the post-depositional history. We performed inverse
195 thermal-history modeling in HeFTy (Ketcham, 2005, 2024) with input uncertainties of 20 % to ensure finding T-t paths compatible with all three grains despite their ZHe-age differences. Appendix C describes how we adjusted the modeling procedures to account for differences between whole-grain He-diffusion kinetics and the diffusion kinetics of the volume that the He was extracted from by laser-ablation. We used the radiation-damage-independent diffusion parameters of Reiners et al. (2004) because the dose-equivalent α -radiation-damage densities of our grains (20 to $120 \cdot 10^{16} \alpha/\text{g}$, measured by Raman
200 spectroscopy) are well within the range for radiation-damage-independent He diffusion (~ 5 to $200 \cdot 10^{16} \alpha/\text{g}$, Guenther et al., 2013). Supplement Table T3 lists the T-t constraints we set for the inverse thermal-history models, including the geologic observation of Lower Cretaceous strata unconformably overlaying the Imperial Formation. We set the stopping condition for the Monte-Carlo-based T-t inversion in HeFTy to 250 good-fit paths (goodness-of-fit > 0.5).

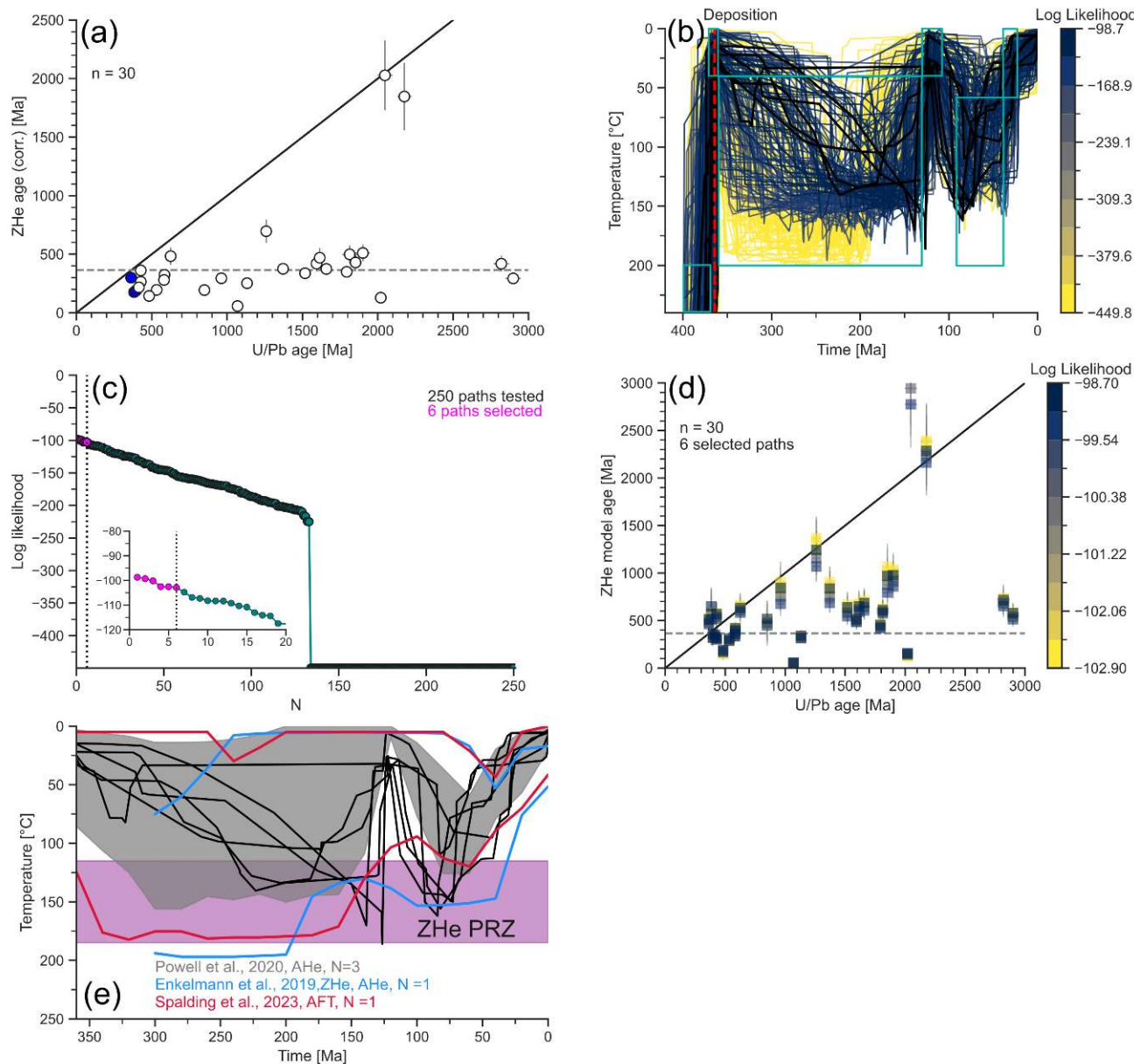


Figure 3: Zircon U/Pb-(U-Th)/He (ZHe) data and modeling results for an Imperial Formation sandstone from the Northern Canadian Cordillera. (a) Plot of measured ZHe vs. U/Pb concordia ages with equal-age (solid), and depositional-age (dashed) lines. Blue symbols: syn-depositional grains. Bars show 2s uncertainties. (b) Temperature-time (T-t) paths from inverse modeling of syn-depositional grains color-coded by log-likelihood. Light-blue boxes: Modeling constraints (Supplement Table T3). Black lines: best-fitting model paths. (c) Sorted log-likelihoods of model paths. The inset shows the region of the 20 highest-likelihood paths. Dotted line: cutoff for the selected best-fitting models (pink circles). (d) Plot of pre-depositional model ZHe ages vs. U/Pb concordia ages for the selected paths color-coded by log-likelihood. Lines and uncertainty bars as in (a). (e) T-t paths of the



selected paths (black lines) compared to envelopes of good-fitting paths from existing thermal-history models (Enkelmann et al., 2019b, blue lines; Powell et al., 2020, grey-shaded area; Spalding et al., 2023; red lines) and the ZHe partial-retention zone (PRZ; purple-shaded area; kinetics of Reiners et al. (2004) for a 30-90 μm grain size). N: number of samples.

For the resulting good-fit paths (Fig. 3b), we calculated the pre-depositional model ages and the path likelihoods. In theory, the syn-depositional grains permit full reset by heating to temperatures >190 °C before 200 Ma (yellow lines), but these paths have low log-likelihoods because they are incompatible with the crystallization ages of the older grains. Most of the other paths (blue and black lines) indicate heating during the Late Paleozoic to Early Mesozoic into the interval between 130 and 180 °C, followed by a second heating event to 50–160 °C in the Late Cretaceous to Paleogene. Out of the 250 paths, the knee-detection algorithm suggests six best-fitting paths (pink circles in Fig. 3c; thick black lines in Fig. 3b). Two of these paths show a first heating phase up to 140 °C in the Triassic, followed by ≥ 50 Myr residence in the ZHe PRZ (purple-shaded area) and cooling in the Jurassic to Cretaceous. Two paths reach their peak temperatures of 140 to 180 °C only in the Late Jurassic to Early Cretaceous before cooling nearly instantaneously. The two final paths do not show heating into the ZHe PRZ before the Late Cretaceous. For the Late-Cretaceous to Paleogene heating event, the best-fitting paths indicate peak temperatures of 100 to 160 °C between 90 and 70 Ma, or about 95 °C at 50 Ma.

Figure 3d plots the pre-depositional model ZHe ages for the six best-fitting paths against the U/Pb ages of our grains. Overall, about 83 % of the grains (25 out of 30 grains) show the expected behavior, falling between the crystallization age (solid line) and the deposition age (dashed line). The main group of pre-depositional model ZHe ages falls in the Neoproterozoic to Paleozoic range, with a single grain straddling the equal-age line at 2.2 Ga. Two of the remaining pre-depositional ages are higher than the respective U/Pb ages, indicating that the diffusion model overestimates their degree of reset relative to the measured ZHe age. One of them is a syn-depositional grain, whose misfit in Fig. 3d reflects the difference between its analytical uncertainty and the expanded uncertainty used for the inverse T-t modeling. Three pre-depositional ages post-date deposition because the diffusion model underestimates their degree of reset. The misfits between modelled and expected ages reflect several simplifications of the diffusion model, which we discuss in section 4.1. Still, the 83 % of the grains overlapping with the expected envelope, confirm that a simple diffusion model can retrieve consistent T-t information from detrital data with a high degree of partial reset.

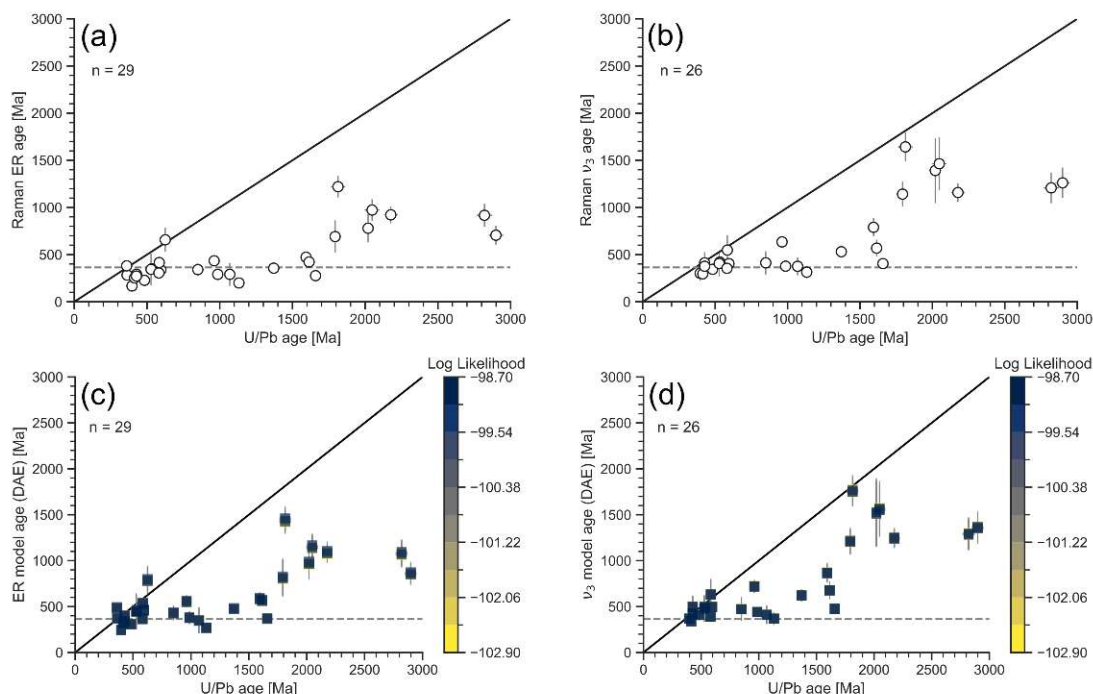


Figure 4: Zircon Raman (ZR) data and pre-depositional model ages for the Imperial-Formation sandstone. (a–b) ZR vs. U/Pb age-age plots for the external rotation (ER; a) and ν_3 (b) Raman bands. (c–d) Plots of pre-depositional model ZR vs. U/Pb ages for the ER (c) and ν_3 (d) bands color-coded by the log-likelihood. The lines denote equal ages (solid), and the depositional age (dashed). The bars show 2s uncertainties.

To further validate our modeling results, we use the zircon Raman (ZR) data from the same grains dated with the U/Pb and ZHe methods. Figures 4a and b plot the measured ZR ages from the ER ($\sim 356 \text{ cm}^{-1}$) and ν_3 ($\sim 1008 \text{ cm}^{-1}$) Raman bands against the U/Pb ages. Zircon Raman ages spread across the depositional age, indicating that these dating systems were partially reset. The lower proportions of post-depositional ages in Figs. 4a and b (ER: 55 %; ν_3 : 19 %) compared to the ZHe ages (73 %) agree with the ZR systems' lower susceptibilities to reset despite their broad partial annealing zones (PAZ; ER: 180 to 450 °C; ν_3 : 220 to 480 °C for 20 to 80 % annealing; Härtel et al., 2021). In addition, both ZR age distributions are bimodal, with a younger population (ER: 200 to 500 Ma; ν_3 : 300 to 800 Ma) of grains that crystallized after 1.8 Ga, and an older population (ER: 700 to 1300 Ma, ν_3 : 1.1 to 1.7 Ga) of grains with U/Pb ages exceeding 1.8 Ga. We determined the pre-depositional model ZR ages based on the distributed-activation-energy kinetic model of Härtel et al. (2021; see Appendix A). Figures 4c and d plot these ages against the U/Pb ages. In general, there is negligible age variation between T-t paths, which is explained by the low sensitivity to temperature differences at the edges of the ZR PAZs. Of the 29 pre-depositional ER ages, 24 (~ 83 %) overlap with the expected age range; only three are lower than the depositional age and do not overlap within uncertainties, while two ages pre-date the U/Pb ages. For the ν_3 band, all pre-depositional ages overlap with the



240 expected age range within uncertainty. For both ZR ages, the pre-depositional ages preserve their bimodal distributions with the younger group ranging from the depositional age to 800 Ma (ER) and 900 Ma (v_3), and the older group spanning from 800 to 1500 Ma (ER) and from 1.2 Ga to 1.8 Ga (v_3). The overall good fits of the pre-depositional model ZR ages to the expected age range confirm the consistency of the modeled T-t paths based on He-diffusion kinetics with the measured ZR ages and the radiation-damage-annealing kinetics.

245 While a geological interpretation of the T-t paths and pre-depositional ages for this Devonian sandstone is outside the scope of this paper, we compare our modeling results to existing thermal-history models from the Imperial Formation. Figure 3e plots our best-fitting T-t paths (black lines) together with the envelopes of good-fit T-t paths determined by Enkelmann et al. (2019b; blue lines; apatite (U-Th-Sm)/He (AHe) and ZHe data), Powell et al. (2020; grey-shaded area; AHe data with T-t constraints from ZHe forward- and apatite fission-track (AFT) inverse-modeling results and stratigraphy), and Spalding et al. (2023; red lines; AFT data) – these thermal-history models used a total of five samples within 60 km from our sample location. In general, our best-fitting paths fall into the comparison envelopes, but they show three important deviations: (1) for the Carboniferous–Early Cretaceous part of the thermal history, our best-fitting paths mostly fall into the comparison envelopes, but show less temperature variation, likely due to the U/Pb and depositional ages not allowing heating into the ZHe PRZ before the Triassic (Fig. 3b). (2) Some of our T-t paths indicate higher temperatures during the Early Cretaceous, however, this is likely due to different constraints used for each of the models. (3) Our temperatures for the Late Cretaceous–Paleogene heating event are higher than for the models of Powell et al. (2020) and Spalding et al. (2023), but only two of our paths exceed the temperatures suggested by the models of Enkelmann et al. (2019b). This is likely the result of Powell et al. (2020) and Spalding et al. (2023) mostly relying on lower-temperature chronometers, which are difficult to reconcile with some of the strongly reset ZHe data. Overall, while our T-t paths match previous modeling results from the Imperial Formation, our modeling approach could benefit further from using lower-temperature thermochronometers to better constrain post-reset cooling.

260 The pre-depositional ages also allow comparison to provenance and source-cooling interpretations of the Imperial Formation. The Imperial Formation is part of the Ellesmerian clastic wedge, representing a mixture of sources from the Canadian Shield and Proterozoic to Paleozoic terranes that collided with Laurentia in the Late-Devonian to Mississippian Ellesmerian orogeny (Hadlari et al., 2009; Beranek et al., 2010; Lemieux et al., 2011). Our pre-depositional ZHe ages (Fig. 3d) form a broad continuous distribution from the Neoproterozoic to the Paleozoic, and thus do not contradict Archean to Devonian sources that were partially to fully reset during the Ellesmerian orogeny. The bimodal pre-depositional ZR ages (Figs. 4c and d) separate the cooling of the Canadian Shield in the Paleo- to Mesoproterozoic (older population) from Neoproterozoic to Paleozoic cooling in the younger source terranes (younger population), with a potential minor overprint during the Ellesmerian orogeny. The ZR ages of the younger grain population also overlap strongly with muscovite $^{40}\text{Ar}/^{39}\text{Ar}$ ages of Powell and Schneider (2013) from the Imperial formation, which mostly range from 370 to 640 Ma. The similar closure temperatures (muscovite $^{40}\text{Ar}/^{39}\text{Ar}$: 350 to 400 °C, Harrison and Zeitler, 2005; ER: 260 to 310 °C, v_3 : 330 to 370 °C,

270



Härtel et al., 2021), suggest comparable thermal histories for the zircon and muscovite source rocks. All in all, our modeling results match the existing thermochronological data from the Imperial Formation in the Mackenzie Plain.

4 Discussion

275 While the results show the overall viability of our modeling approach for partially reset samples, it also has some limitations. In the following section, we address the limitations and simplifying assumptions of our approach and their practical implications. Then we discuss the application of our modeling approach to other thermochronometers. Finally, we compare the possibilities of partial-reset modeling to strategies avoiding partially reset samples.

4.1 Limitations of the proposed modelling approach

280 Our modeling strategy successfully leverages the information contained in syn-depositional grains to disentangle pre- and post-depositional thermal histories, but there are three limits that could hamper its use: first, the presence of syn-depositional grains is the method's Achilles heel. This is not critical for analyzing strata that were sourced from regions with coeval magmatic activity (e.g. magmatic arcs, rift magmatism), but it complicates matters for strata with source regions where most of the datable zircon grains are eroded from significantly older rocks (e.g., cratons, metamorphic hinterland; Cawood et al.,
285 2012). It is, however, possible to screen the sample for syn-depositional or near syn-depositional grains first. Daniels et al. (2018) applied U/Pb analysis by LA-ICP-MS with short ablation pulses (e.g., 5 s) to a large number of detrital grains ($n \geq 600$) to find the youngest age population and define a maximum-depositional age. Such a screening approach can be carried out before polishing the grains to the full depth and performing double- or multi-dating. This procedure provides additional U/Pb information from grain rims and offers the prospect of recognizing syn-depositional overgrowths on inherited cores
290 from magmatic sources (Malusà et al., 2022). On the other hand, laser-ablation-based ZHe dating has a decisive advantage over conventional whole-grain ZHe dating for addressing samples with few syn-depositional grains, as it allows acquiring dozens to hundreds of U/Pb-ZHe age pairs without a selection bias toward syn-depositional grains. If no geo- and thermochronometric data from syn-depositional grains can be obtained, it is still possible to use other grains for inverse-thermal history modeling, given that their pre-depositional thermal history is constrained well enough. The most promising
295 way to achieve this—although restricted to coarse clastic deposits—is by analyzing zircon from clasts instead of detrital grains (e.g., Rahl et al., 2011; Grabowski et al., 2013; Falkowski et al., 2016; Stevens Goddard et al., 2024). The main advantage is that other thermochronometers on different minerals or information on the source of the clast can be used together to constrain the pre-depositional thermal history well enough and model the post-depositional history.

300 Second, while our data show that the modeling strategy performs well at a high degree of partial ZHe reset, it becomes less useful once a sample approaches full reset. In this case, the inverse T-t modeling step will find many good-fit paths that lead to full reset. This increases the number of paths necessary for forward-modeling to find solutions that are compatible with the crystallization and depositional ages. In addition, the uncertainty on the pre-depositional model ages increases while reset

erases information on the pre-depositional history. This weakens the log-likelihood criterion for model evaluation and hampers the interpretation of source cooling.

305 Third, our modeling example in section 3 relies on several simplifying assumptions that affect model accuracy, but can be dealt with in the future: (1) we assume a uniform U and Th concentration. Uranium and thorium zoning is common in zircon (e.g., Corfu et al., 2003). It determines He-concentration gradients and thus diffusion rates (e.g., Meesters and Dunai, 2002). If information on zoning is available, e.g., from U-Th mapping, it can easily be incorporated into the inverse- and forward-modeling routines by calculating the He accumulation profile based on the U and Th distributions. (2) We did not take into
310 account effects of inherited radiation-damage. In our case, this decision was supported by low radiation-damage densities directly measured by Raman spectroscopy. For samples containing grains with potentially high degrees of inherited radiation damage, we suggest to incorporate the damage-diffusivity relationship in the forward-modeling step (e.g., using the zircon-radiation-damage-and-annealing model, ZRDAAM; Guenther, 2021). (3) For modeling the retention of pre-depositional He during post-depositional heating, we assumed that the initial He-concentration profile within the grain was similar to an α -
315 ejection profile. While this is not necessarily the case, we regard it as a reasonable estimate: if diffusion rounding of the He concentration profile occurred before deposition, it is at least in part diluted toward an α -ejection profile during pre-depositional cooling. Hence, the true He-concentration profile will only differ significantly from an α -ejection profile for a sample that first accumulated a large amount of He prior to deposition, was reheated to temperatures within the PRZ, and cooled immediately before deposition. Nevertheless, it is possible to adjust the pre-depositional He profile in the modeling
320 procedure, e.g., to account for the effect of abrasion during transport. For abraded grains, the He-accumulation profile at the time of deposition falls between two endmembers (see Rahl et al., 2003): either the grains were abraded a long time before deposition and developed an α -ejection profile with respect to its present-day grain boundary, or their complete α -ejection profile was abraded very close to the time of deposition. It is therefore possible to determine a pre-depositional-age envelope for the abraded grains by using two different He-concentration profile, one with and one without α -ejection rim. (4) We
325 assumed approximate ablation-pit positions within the grain for the laser-ablation ZHe data in section 3 and placed them directly in the spherical transformations of our grains (Appendix C). Accurate measurements of the pit positions relative to the 3D grain boundaries would allow the translation of the pit volume to spherical coordinates. Sampling the modeled He concentrations from this translated volume would improve the accuracy of both, the inverse and forward-modeling steps.

4.2 Other thermochronometers

330 The focus of our modeling approach is on zircon U/Pb-(U-Th)/He double-dating, but the overall strategy can also be applied to other thermochronometers. For samples partially reset with respect to the AHe system, the combination with apatite U/Pb dating can be applied in the same way. While the apatite U/Pb system is more susceptible to Pb loss by thermally activated diffusion than the zircon U/Pb system, its temperature-sensitivity window (closure temperature \approx 350 to 570 °C; Cherniak, 2010) is much higher than that of the AHe PRZ (40 to 80 °C; Farley, 2000). Hence, the apatite U/Pb age allows the
335 identification of grains that formed or cooled from sufficiently high temperatures processes shortly before deposition.



Compared to zircon, apatite is less mechanically and chemically stable (Morton, 1982; Jess et al., 2023), making it more useful for tracing the provenance and cooling histories of first-cycle sediment sources. In addition, its chemical composition is more diagnostic for source-rock lithologies (e.g., O’Sullivan et al., 2020).

Another double-dating scheme, for which partial-reset modeling holds great potential, is combined U/Pb and fission-track dating, particularly in the light of the laser-ablation-based fission-track dating technique (e.g., Hasebe et al., 2004). Fission-track dating is popular for detrital thermochronology due to the time- and cost-efficient data acquisition for large samples and its compatibility with U/Pb dating (e.g., Garver et al., 1999; Bernet and Garver, 2005; Chew and Donelick, 2012; Enkelmann et al., 2019a). Besides the ages, confined-track-length distributions in apatite are a powerful tool for thermal-history modeling (e.g., Green, 1988; Duddy et al., 1988; Ketchum, 2005). Still, for partially reset samples, the uncertainty about each grain’s pre-depositional thermal history complicates the interpretation of AFT data (e.g., Fillon et al., 2013). A suggested solution to this problem uses the relative age of confined tracks with respect to their length for distinguishing pre- and post-depositional tracks and modeling the post-depositional thermal history (e.g., Keil et al., 1987; Jensen and Hansen, 2021; Jensen et al., 1992). However, this approach requires a large-enough number of post-depositional fission tracks, which is a potential problem for post-Paleozoic sedimentary samples or samples containing relatively U-poor apatite grains. In contrast, translating our strategy to U/Pb-fission-track double-dating would allow constraining the post-depositional thermal history from apatite or zircon fission-track ages of the syn-depositional grains. For AFT samples with large numbers of confined tracks, the track lengths of the syn-depositional grains could even provide a high-resolution post-depositional thermal history.

4.3 Partial-reset modeling vs. unreset or fully reset samples

The above discussion raises a question: (when) is modeling partially reset detrital samples necessary? This depends first and foremost on the geological question to be addressed, e.g., if one aims to determine the cooling history of source rocks, the sediment-burial depth, or both. To determine cooling ages of source regions, relying on an undisturbed, higher-temperature thermochronometer is a viable strategy. However, this risks opening a large temporal gap between source-region cooling and deposition, potentially overlooking relevant lower-temperature processes. On the other hand, a fully reset low-temperature tracks cooling in the basin, but only provides a rough estimate for the maximum-burial temperature. Avoiding partial reset also requires additional temperature information, e.g., from stratigraphy, thermal maturation of the analyzed strata, or metamorphic grades in the source regions.

In contrast, the possibility of extracting thermal histories by partial-reset modeling allows analyzing samples with different degrees of reset, e.g., in a stratigraphic succession, without changing chronometers. In addition, a partially reset thermochronometer is most sensitive to heating and cooling in the temperature window the sample reached after deposition. It thus offers the unique opportunity of determining the temperature-time relationship of post-depositional heating in more detail than a fully reset chronometer. It also records source cooling through relatively low temperatures, narrowing the gap



370 between cooling and deposition. Finally, the possibility of partial-reset modeling eliminates the need for additional information on post-depositional temperature while still benefitting from other thermochronological, sedimentological, or thermal-maturation data.

5 Conclusions

In this paper, we describe a new modeling strategy for interpreting partially reset zircon (U-Th)/He (ZHe) data from sedimentary samples using combined ZHe and U/Pb dating on individual grains. It uses the U/Pb ages to find syn-depositional grains and determines the post-depositional thermal history from inverse temperature-time modeling based on these grains. It then proceeds by forward-modeling the post-depositional history and determining model pre-depositional ages for each grain. The evaluation of temperature-time (T-t) paths rests on their predicted pre-depositional ages falling into the expected interval between U/Pb and depositional age. Applying this strategy to combined U/Pb-ZHe data from a Devonian sandstone from the Northern Canadian Cordillera gives results that are internally consistent and agree with existing thermochronological data. Our approach is further validated by data from the higher-temperature and thus less-reset zircon Raman (ZR) dating system and pre-depositional ZR ages match existing muscovite $^{40}\text{Ar}/^{39}\text{Ar}$ data from the Imperial Formation. While leveraging the thermal-history information from syn-depositional grains allows us to separate the pre- and post-depositional histories, it also limits our modeling approach to samples containing such grains. On the other hand, compared to other modeling approaches, our strategy does not require specific assumptions on the pre-depositional thermal history. In addition, calculating pre-depositional ages on a grain-by-grain basis allows to compare them to other single-grain data relevant for provenance. Our approach uses a simple He-diffusion model, but other factors such as U and Th zoning, radiation damage, or grain abrasion can be integrated into the modeling procedure. While this paper focuses on zircon U/Pb-ZHe double-dating or multi-dating including zircon Raman data, the general principles of the modeling approach can be directly translated to combined apatite U/Pb and (U-Th-Sm)/He or fission-track dating.



Appendix A: Model setup for pre-depositional age calculation

390 Our forward-model for estimating the fraction of retention and the He accumulated after deposition used a radial diffusion model in spherical geometry. We first translated the dimensions of the analyzed grains to an equivalent spherical radius, using the equation of Ketcham et al. (2011) for a cylindrical shape and divided the radial profile into a discrete number of nodes. To determine the relative proportion of He produced at each radial distance from the center, we determined the α -ejection profile by Monte-Carlo simulation. The stopping distances were calculated in SRIM 2013 (Ziegler, 2013) based on disintegration energies of Haynes et al. (2014), excluding those energies occurring for <1 % of the parent nuclide's decay events. To estimate the respective contributions from the ^{238}U , ^{235}U and ^{232}Th decay chains, we used the measured Th/U ratios, assuming uniform U and Th concentrations throughout the grains.

The next step was to cut and simplify the post-depositional temperature-time (T-t) paths provided by the inverse modeling in HeFTy (v. 2.17; Ketcham, 2005, 2024). First, we interpolated the T-t paths to short (e.g., 2 Myr) isothermal segments between deposition and the present day. The lower limit of the depositional-age constraint from HeFTy was used to exclude pre-depositional cooling from the forward-models. We summarized consecutive steps with small temperature differences (e.g., 5 °C) in each T-t path by integrating the temperature-dependent diffusion coefficient D (e.g., Lovera et al., 1989):

$$\int_{t_i}^{t_{i+2}} D(T(t)) dt = D_{i,i+1} (t_{i+2} - t_i) \quad (\text{A1}),$$

with t_i being the starting time of the i th time step.

405 The HeFTy modeling from the syn-depositional grains allows T-t paths leading to fully reset. As such solutions are at odds with the observation of a partially reset sample, we filtered out all fully reset paths based on an estimate for the total degree of post-depositional reset. We based this estimate on D_{total} each path's T-t conditions integrated into a single time step using eq. (A1). The remaining pre-depositional He concentration depends on the normalized step length F :

$$F = \frac{\sqrt{D_{total} t_{total}}}{R} \quad (\text{A2}),$$

410 where t_{total} is the total time of the thermal history and R is the equivalent spherical grain radius. The analytical equation for the ratio of He retained after the thermal history, ϕ_{post} , is (Jost, 1952; Fechtig et al., 1961):

$$\phi_{post} = \frac{6}{\pi^2} \sum_{n=1}^{\infty} \frac{1}{n^2} e^{-n^2 \pi^2 F^2} \quad (\text{A3}).$$

Figure A1 shows the decrease of ϕ_{post} with increasing F . We identified the paths with a median F of 0.75 ($\phi_{post} < 0.3\%$) among the analyzed grains as full-reset paths and set all their pre-depositional ages to zero.

415 We determined the degree of post-depositional He retention ϕ_{post} by forward-modeling He diffusion using t_{total} and D_{total} . The He concentration was determined at every node in the radial profile using the Crank-Nicolson algorithm (Crank and Nicolson, 1947) with a Neumann boundary at the center (constant concentration gradient) and a Dirichlet boundary at the grain rim (infinite He sink).

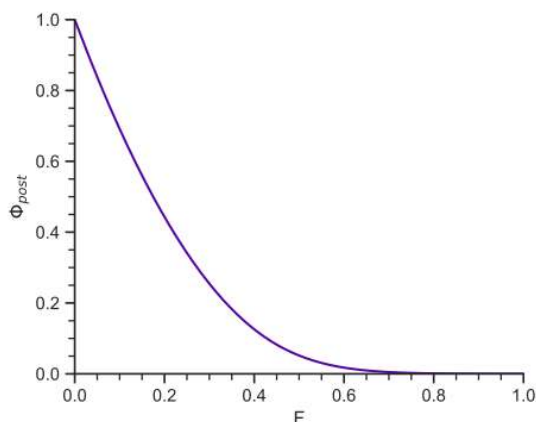


Fig. A1: Relationship between the post-depositional He retention ϕ_{post} and the normalized step length F .

420 We used the kinetic parameters of Reiners et al. (2004) for non-metamict zircon, however, it is possible to use other models such as the zircon-radiation-damage-and-annealing model (ZRDAAM, Guenther et al., 2013, 2015; Guenther, 2021). We calculated the fraction of post-depositional retention ϕ_{post} as the ratio of the remaining concentration $C_{\text{loss only}}$ to the starting concentration C_{initial} . The whole-grain concentrations C are the radially weighted sums of the concentration C_r at the radial distance r from the grain center:

$$C = \sum_{r=0}^{r=R} w_r C_r \quad (\text{A4}),$$

425 The weight w_r at radius r is:

$$w_r = 4 \pi r^2 dr \quad (\text{A5}).$$

dr is the radial distance between the He-concentration nodes.

We modeled the amount of He accumulated during the post-depositional thermal history with He production and diffusion at each step of the simplified T-t history. The He production used the relative concentrations of the α -ejection profile scaled by the He accumulation rate depending on the changes in U and Th concentrations over geologic time. We determined the pre-depositional He concentration from the observed He concentration and the modeling results using eq. (3) and calculated the pre-depositional model age from eq. (4) by iteration of the effective uranium concentration (eU; Härtel and Enkelmann, 2024; their Appendix A) based on the U and Th concentrations at the time of deposition. For α -ejection correction, we scaled the final He-concentration profile against the α -ejection profile. To approximate the model-age uncertainty, we divided the observed ZHe age uncertainty by ϕ_{post} . We tested the validity of our diffusion model against the analytical equation for volume diffusion from a spherical grain (eq. (A3)) and the accumulation and age-calculation procedures against synthetic accumulation-only thermal histories.

430
435



For the zircon Raman ages in section 3, we first interpolated the HeFTy paths to isothermal segments as for the ZHe model. We applied an equivalent-time-based modeling approach (Duddy et al., 1988) similar to that of Guentner (2021) for radiation-damage forward-modeling. The principle of equivalent time assumes that future daughter loss only depends on the future T-t conditions and the current degree of reset, but not the specific past T-t history. This implies that any segment of a given T-t history can be translated to a different temperature-time pair that causes an equivalent degree of reset, which facilitates dealing with complicated thermal histories. Let the post-depositional history comprise k isothermal steps with temperature T_i and duration Δt_i . f_i is the cumulative degree of fractional annealing a portion of daughters produced in the i th step for all steps $\geq i$. The reset duration $\Delta\tau_{res,i}$ is then the time necessary to reach f_i by isothermal holding at T_i . f_i follows from the reset function $R(t, T)$:

$$f_i = R(\Delta\tau_{res,i}, T_i) \quad (\text{A6}).$$

$\Delta\tau_{res,i}$ is easily defined for the last time step k , where it simply equals the duration Δt_k :

$$\Delta\tau_{res,k} = \Delta t_k \quad (\text{A7}).$$

The radiation-damage produced at the second-last step $k-1$ underwent the combined thermal history of steps $k-1$ and k . Its reset duration $\Delta\tau_{res,k-1}$ follows from the duration of step $k-1$ and the equivalent time $\Delta\tau_{eq}$:

$$\Delta\tau_{res,k-1} = \Delta t_{k-1} + \Delta\tau_{eq}(\Delta t_k, T_k, T_{k-1}) \quad (\text{A8}).$$

$\Delta\tau_{eq}$ is the time needed to reach the degree of reset of the k th step $R(\Delta t_k, T_k)$ at temperature T_{k-1} :

$$R(\Delta\tau_{eq}(\Delta t_k, T_k, T_{k-1}), T_{k-1}) = R(\Delta t_k, T_k) \quad (\text{A9}).$$

f_i then follows from eq. (A9) and $\Delta\tau_{res,i}$ of each previous step:

$$f = \left[R(\Delta\tau_{res,1}, T_1); \dots; R(\Delta\tau_{res,k}, T_k) \right] \quad (\text{A10}).$$

We determined the post-depositional fraction of damage retention equals from the degree of annealing of the first time step. The post-depositional damage density $D_{postdep}$ is the scalar product of the duration vector τ , the vector f of the fractions of reset at each time step, and ρ , the vector of damage-production rates at each time step:

$$D_{postdep} = \tau * f * \rho \quad (\text{A11}).$$

We calculated the pre-depositional model zircon Raman ages from eq. (4). For the radiation-damage modeling, we assumed that most of the lattice damage present at the time of deposition behaved as unannealed, i.e. that no significant annealing took place immediately before deposition, analogous to the assumption of an α -ejection profile (section 4.1). We used the damage-annealing kinetics following the distributed-activation-energy model of Härtel et al. (2021b) but other radiation-damage annealing models (e.g., Geisler et al., 2001; Ginster et al., 2019) can also be used, as long as the activation energy of the annealing process is not a function of time (Duddy et al., 1988; Rufino et al., 2023).



Appendix B: Calculation of Likelihoods for each tested T-t path

To evaluate the T-t paths determined by HeFTy, we calculated the path likelihood L_i for the i th grain as the probability of the pre-depositional model age $t_{p,i}$ falling between the U/Pb age $t_{U/Pb,i}$ and the depositional age t_{dep} :

$$L_i = Pr(t_{dep} < t_{p,i} < t_{U/Pb,i}) \quad (B1).$$

This likelihood is approximately the integral of a Gaussian function with the mean at the model age and the model-age uncertainty as standard deviation in the limits of the U/Pb and depositional age (grey-shaded area in Fig. B1).

To include uncertainties on the U/Pb and depositional ages, we determined the likelihoods in a Monte Carlo approach. We sampled n values (here 1,000,000) for $t_{p,i}$, $t_{U/Pb,i}$, and t_{dep} from normal distributions with ages as means and 1s uncertainties as standard deviations and calculated the likelihood by dividing the number of cases, in which $t_{p,i}$ falls between the other two by n . For grain-thermal-history combinations, in which none of the iterations matched the expected envelope, we set the likelihood to that of half a match. This procedure for calculating the individual-grain likelihoods has several consequences: (1) it penalizes models producing pre-depositional ages outside the expected age envelope. (2) The single-grain likelihoods are relatively constant within the expected envelope, so that no pre-depositional cooling age within the allowed range is preferred over another. (3) The discrete lower limit of the single-grain likelihoods assigns a constant likelihood to model ages far from the expected age interval. Therefore, they lose influence on the model selection once they reach a certain distance from this envelope.

We then determined the total log-likelihood LL of each T-t path as the sum of the logarithmized individual likelihoods.

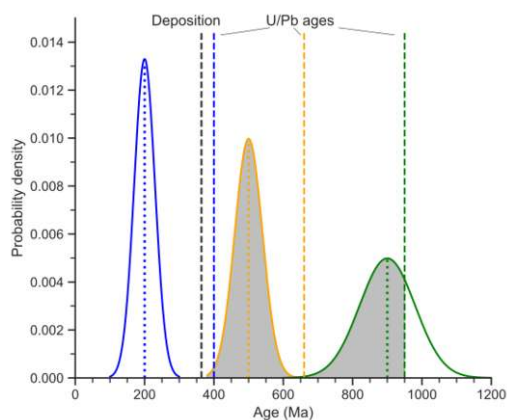


Figure B1: Probability-density plot illustrating the assignment of likelihoods to model paths on three grains with Gaussian bell curves describing the pre-depositional model ages (dotted lines) and uncertainties and the dashed lines representing the U/Pb and depositional ages. Shaded areas: model-age density in the expected age envelope.



Appendix C: Adapting the zircon (U-Th)/He diffusion model to laser-ablation-based dating

485 To adapt our modeling strategy to the laser-ablation-based in-situ zircon (U-Th)/He (ZHe) data in section 3, we modified the
 inverse- and forward-modeling algorithms to only evaluate the part of the He-concentration profile that corresponds most
 closely to the position of the laser-ablation pit, from which He was extracted. In the absence of precise measurements, we
 determined pit positions using the following criteria: (1) we assumed spherical grains; (2) we assumed that the pits were
 centered on the centers of the horizontal polished grain sections; (3) for grains that were drilled through during the U and Th
 490 analysis by LA-ICP-MS, we determined the vertical position of the He-extraction pit from the distance of its floor to the
 bottom of the grain (see Härtel et al., 2026); (4) for the other grains, we estimated the vertical position of the pit based on the
 amount of material polished away during sample preparation (20 μm ; Härtel et al., 2026). Based on the pit position, the grain
 size and the average pit shape and size (a truncated cone with a radius of 8 μm at the polished surface, pit walls at an angle
 of 22 $^\circ$ to vertical, and a depth of 6.6 μm), we determined the volume distribution of the He-extraction pit in every grain as a
 495 function of the distance from the grain center by Monte-Carlo simulation.

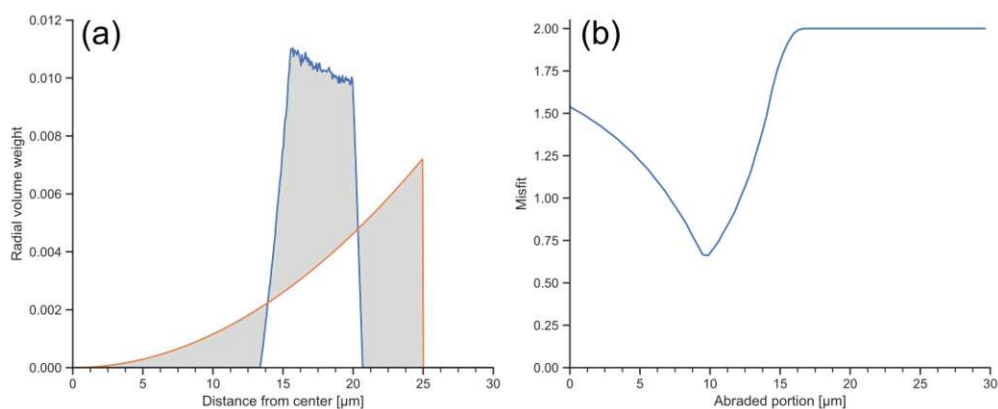


Figure C1: Comparison of the volume-weighted radial positions of He-extraction pits from laser ablation and spherical cores of abraded grains. (a) Radial-volume-weight curves for the laser-ablation pit (blue) in a 30- μm radius zircon grain and the abraded core after 5 μm abrasion (orange). The shaded areas mark radial regions of misfit. (b) Plot of misfit between radial curves as in (a) as a function of the abraded portion.

We used this information for the inverse- and forward-modeling steps of our analysis. For the inverse modeling in HeFTy, we estimated an “abraded” parameter based on the volume distributions of the pits in the syn-depositional grains. This option in HeFTy assumes a spherical post-abrasion core. We therefore determined the size of a sphere surrounding the grain center, whose volume distribution relative to the grain center is as close to that of the ablation spot as possible. Figure C1a illustrates
 500 the volume distributions of an ablation pit (blue line; geometry as above, 10 μm distance from the grain bottom) for a grain with a spherical radius of 30 μm and an abraded core with 25 μm radius (orange line). We evaluated the misfit between the two distributions as the sum of the absolute areas between the curves (grey shaded areas). This value varies between 0 for a



perfect match and 2 for two distributions that do not overlap. Figure C1b is a plot of the misfit of the ablation pit in Fig. C1a
against different abraded depths for a grain with 30 μm radius. The global minimum of misfit is at about 10 μm and rapidly
505 increases toward lower and higher values. We used the abraded portions for the minimum misfits as “abraded” values as
inputs in HeFTy. For the forward modeling, we determined ϕ_{post} and He_{post} by modeling each grain and then sampling He
from the concentration profiles based on the volume distributions of the He-extraction pits. We also used these volume
distributions to correct the pre-depositional He concentrations for α -ejection.

Code and data availability

510 The synthetic U/Pb and zircon (U-Th)/He data shown in Fig. 2 and their true thermal histories are available in Supplement
Tables T1 and T2 to this article. The U/Pb and zircon (U-Th)/He and zircon Raman data in Figs. 3 and 4 are from the
Supplementary Material of Härtel et al. (2026; <https://doi.org/10.1016/j.chemgeo.2026.123435>). PaRACAS is available as a
jupyter notebook at <https://doi.org/10.5281/zenodo.18248225>.

Author contributions

515 BPH, EE, and AM contributed to the conceptualization of the study. BPH and AM carried out the formal analysis. BPH
developed the software. BPH and EE acquired the funding. BPH wrote the manuscript with contributions from the co-
authors.

Competing interests

The authors declare that they have no conflict of interest.

520 Acknowledgements and Funding

This research was funded by the Natural Sciences and Engineering Research council (NSERC) grant RGPIN-2024-03863
and by the donors of ACS Petroleum Research Fund under New Directions Grant PRF# 67107-ND8. EE served as Principal
Investigator on PRF# 67107-ND8 that provided support for BPH and AM. BPH acknowledges funding by the a German
Research Council (Deutsche Forschungsgemeinschaft) Walter-Benjamin fellowship (HA 9685/1-1).



525 References

- Beranek, L.P., Mortensen, J.K., Lane, L.S., Allen, T.L., Fraser, T.A., Hadlari, T., and Zantvoort, W.G.: Detrital zircon geochronology of the western Ellesmerian clastic wedge, northwestern Canada: insights on Arctic tectonics and the evolution of the northern Cordilleran miogeocline, *Geol. Soc. Am. Bull.*, 122, 1899–1911, <https://doi.org/10.1130/B30120.1>, 2010.
- 530 Bernet, M., and Garver, J.I.: Fission-track analysis of detrital zircon, *Rev. Mineral. Geochem.*, 58, 205–238, <https://doi.org/10.2138/rmg.2005.58.8>, 2005.
- Bootes, N., Enkelmann, E., and Lease, R.: Late Miocene to Pleistocene source to sink record of exhumation and sediment routing in the Gulf of Alaska from detrital zircon fission-track and U-Pb double dating, *Tectonics*, 38, 2703–2726, <https://doi.org/10.1029/2019TC005497>, 2019.
- 535 Boyce, J.W., Hodges, K.V., Olszewski, W.J., Jercinovic, M.J., Carpenter, B.D., and Reiners, P.W.: Laser microprobe (U-Th)/He geochronology, *Geochim. Cosmochim. Acta*, 70, 3031–3039, <https://doi.org/10.1016/j.gca.2006.03.019>, 2006.
- Carlson, W.D., Donelick, R.A., and Ketcham, R.A.: Variability of apatite fission-track annealing kinetics; I, Experimental results, *Am. Miner.*, 84, 1213–1223, <https://doi.org/10.2138/am-1999-0901>, 1999.
- 540 Carter, A., and Moss, S.J.: Combined detrital-zircon fission-track and U-Pb dating: A new approach to understanding hinterland evolution, *Geology*, 27, 235–238, [https://doi.org/10.1130/0091-7613\(1999\)027<0235:CDZFTA>2.3.CO;2](https://doi.org/10.1130/0091-7613(1999)027<0235:CDZFTA>2.3.CO;2), 1999.
- Carrapa, B., DeCelles, P.G., Reiners, P.W., Gehrels, G.E., and Sudo, M.: Apatite triple dating and white mica $^{40}\text{Ar}/^{39}\text{Ar}$ thermochronology of syntectonic detritus in the Central Andes: A multiphase tectonothermal history, *Geology*, 37, 407–410, <https://doi.org/10.1130/G25698A.1>, 2009.
- 545 Cawood, P.A., Hawkesworth, C.J., and Dhuime, B.: Detrital zircon record and tectonic setting, *Geology*, 40, 875–878, <https://doi.org/10.1130/G32945.1>, 2012.
- Cecil, M.R., Saleeby, Z., Saleeby, J., and Farley, K.A.: Pliocene–Quaternary subsidence and exhumation of the southeastern San Joaquin Basin, California, in response to mantle lithosphere removal, *Geosphere*, 10, 129–147, <https://doi.org/10.1130/GES00882.1>, 2014.
- 550 Cherniak, D.J., 2010: Diffusion in accessory minerals: zircon, titanite, apatite, monazite and xenotime, *Rev. Mineral. Geochem.*, 72, 827–869, <https://doi.org/10.2138/rmg.2010.72.18>, 2010.
- Chew, D., and Donelick, R.A.: Combined apatite fission track and U-Pb dating by LA-ICP-MS and its application in apatite provenance analysis, in: *Quantitative mineralogy and microanalysis of sediments and sedimentary rocks*, edited by Sylvester, P., Mineralogical Association of Canada, Sudbury, 219–247, <https://doi.org/10.3749/9780921294825.ch12>, 2012.
- Corfu, F., Hanchar, J.M., Hoskin, P.W.O., and Kinny, P.: Atlas of zircon textures, *Rev. Mineral. Geochem.*, 53, 469–500, <https://doi.org/10.2113/0530469>, 2003.
- 560 Crank J., and Nicolson P., 1947: A practical method for numerical evaluation of solutions of partial differential equations of the heat-conduction type, *Math. Proc. Camb. Phil. Soc.*, 43, 50–67, <https://doi.org/10.1017/S0305004100023197>.
- Daniels, B.G., Auchter, N.C., Hubbard, S.M., Romans, B.W., Matthews, W.A., and Stright, L.: Timing of deep-water slope evolution constrained by large-n detrital volcanic ash zircon geochronology, Cretaceous Magallanes Basin, Chile, *Geol. Soc. Am. Bull.*, 130, 438–454, <https://doi.org/10.1130/B31757.1>, 2018.
- Danišik, M.: Integration of fission-track thermochronology with other geochronologic methods on single crystals, in: *Fission-track thermochronology and its application to Geology*, edited by Malusà, M.G., and Fitzgerald, P.G., Springer International Publishing, New York, 93–108, https://doi.org/10.1007/978-3-319-89421-8_5, 2019.
- 565 Duddy, I.R., Green, P.F., and Laslett, G.M.: Thermal annealing of fission tracks in apatite 3. Variable temperature behaviour, *Chem. Geol.*, 73, 25–38, [https://doi.org/10.1016/0168-9622\(88\)90019-X](https://doi.org/10.1016/0168-9622(88)90019-X), 1988.
- Dunkl, I., Mallis, F., Lünsdorf, N.K., Schönig, J., and von Eynatten, H.: Zircon U-Pb-He double dating of modern sands from the Inn River catchment: assessing resolution and potential in a complex orogenic setting, *J. Geophys. Res. Earth Surf.*, 129, e2023JF007360, <https://doi.org/10.1029/2023JF007360>, 2024.
- 570 Enkelmann, E., Garver, J.I., and Pavlis, T.L.: Rapid exhumation of ice-covered rocks of the Chugach–St. Elias orogen, Southeast Alaska, *Geology*, 36, 915–918, <https://doi.org/10.1130/G2252A.1>, 2008.



- 575 Enkelmann, E., Ridgway, K.E., Carignano, C., and Linnemann, U.: A thermochronometric view into an ancient landscape: tectonic setting, development, and inversion of the Paleozoic eastern Paganzo basin, Argentina, *Lithosphere*, 6, 93–107, <https://doi.org/10.1130/L309.1>, 2014.
- Enkelmann, Sanchez-Lohff, S.K., Finzel, E.S.: Detrital zircon double-dating of forearc basin strata reveals magmatic, exhumational, and thermal history of sediment source areas, *Geol. Soc. Am. Bull.*, 131, 1364–1384, <https://doi.org/10.1130/B35043.1>, 2019a.
- 580 Enkelmann, E., Finzel, E., and Arkle, J.: Deformation at the eastern margin of the Northern Canadian Cordillera: Potentially related to opening of the North Atlantic, *Terra Nova*, 31, 151–158, <https://doi.org/10.1111/ter.12374>, 2019b.
- Evans, N.J., McInnes, B.I.A., McDonald, B., Danišik, M., Becker, T., Vermeesch, P., Shelley, M., Marillo-Sialer, E., and Patterson, D.B.: An in situ technique for (U-Th-Sm)/He and U-Pb double dating, *J. Anal. Atom. Spectrom.*, 30, 1636–1645, <https://doi.org/10.1039/C5JA00085H>, 2015.
- 585 von Eynatten, H., and Dunkl, I.: Assessing the sediment factory: The role of single grain analysis, *Earth-Sci. Rev.*, 115, 97–120, <https://doi.org/10.1016/j.earscirev.2012.08.001>, 2012.
- Falkowski, S., Enkelmann, E., Drost, K., Pfänder, J.A., Stübner, K., Ehlers, T.A.: Cooling history of the St. Elias syntaxis, southeast Alaska, revealed by geo- and thermochronology of cobble-size glacial detritus, *Tectonics*, 35, 447–468, <https://doi.org/10.1002/2015TC004086>, 2016.
- 590 Farley, K.A.: Helium diffusion from apatite: General behavior as illustrated by Durango fluorapatite, *J. Geophys. Res. Solid Earth*, 105, 2903–2914, <https://doi.org/10.1029/1999JB900348>, 2000.
- Fechtig, H., Gentner, W., and Kalbitzer, S.: Argonbestimmungen an Kaliummineralien—IX: Messungen zu den verschiedenen Arten der Argondiffusion, *Geochim. Cosmochim. Acta*, 25, 297–311, [https://doi.org/10.1016/0016-7037\(61\)90064-3](https://doi.org/10.1016/0016-7037(61)90064-3), 1961.
- 595 Fillon, C., Gautheron, C., and van der Beek, P.: Oligocene–Miocene burial and exhumation of the Southern Pyrenean foreland quantified by low-temperature thermochronology, *J. Geol. Soc. London*, 170, 67–77, <https://doi.org/10.1144/jgs2012-051>, 2013.
- Flowers, R.M., Ketcham, R.A., Shuster, D.L., and Farley, K.A.: Apatite (U-Th)/he thermochronometry using a radiation damage accumulation and annealing model, *Geochim. Cosmochim. Acta*, 73, 2347–2365, <https://doi.org/10.1016/j.gca.2009.01.015>, 2009.
- 600 Flowers, R.M., Ketcham, R.A., Enkelmann, E., Gautheron, C., Reiners, P.W., Metcalf, J.R., Danišik, M., Stockli, D.F., and Brown, R.W.: (U-Th)/He chronology: Part 2. Considerations for evaluating, integrating, and interpreting conventional individual aliquot data, *Geol. Soc. Am. Bull.*, 135, 137–161, <https://doi.org/10.1130/B36268.1>, 2022.
- Forte, A.M., Gutterman, K.R., van Soest, M.C., and Gallagher, K.: Building a young mountain range: insights into the growth of the Greater Caucasus Mountains from detrital zircon (U-Th)/He thermochronology and ¹⁰Be erosion rates, *Tectonics*, 41, e2021TC006900, <https://doi.org/10.1029/2021TC006900>, 2022.
- 605 Fosdick, J.C., Grove, M., Graham, S.A., Hourigan, J.K., Lovera, O., and Romans, B.W.: Detrital thermochronologic record of burial heating and sediment recycling in the Magallanes foreland basin, Patagonian Andes, *Basin Res.*, 27, 546–572, <https://doi.org/10.1111/bre.12088>, 2015.
- 610 Fox, M., Dai, J.-G., and Carter, A.: Badly behaved detrital (U-Th)/He ages: problems with He diffusion models or geological models? *Geochem. Geophys. Geosys.*, 20, 2418–2432, <https://doi.org/10.1029/2018GC008102>, 2019.
- Gallagher, K.: Transdimensional inverse thermal history modeling for quantitative thermochronology, *J. Geophys. Res.* 117, B02408, <https://doi.org/10.1029/2011JB008825>, 2012.
- 615 Garver, J.I., Brandon, M.T., Roden-Tice, M., and Kamp, P.J.J.: Exhumation history of orogenic highlands determined by detrital fission-track thermochronology, in: *Exhumation processes: normal faulting, ductile flow and erosion*, edited by Ring, U., Brandon, M.T., Lister, G.S., and Willett, S.D., *Geol. Soc. Spec. Pub.*, 154, London, 283–304, <https://doi.org/10.1144/GSL.SP.1999.154.01.13>, 1999.
- Geisler, T., Pidgeon, R.T., Van Bronswijk, W., and Pleysier, R.: Kinetics of thermal recovery and recrystallization of partially metamict zircon: a Raman spectroscopic study, *Eur. J. Mineral.*, 13, 1163–1176, <https://doi.org/10.1127/0935-1221/2001/0013-1163>, 2001.
- 620 Ginster, U., Reiners, P.W., Nasdala, L., and Chanmuang N.,C.: Annealing kinetics of radiation damage in zircon, *Geochim. Cosmochim. Acta*, 249, 225–246, <https://doi.org/10.1016/j.gca.2019.01.033>, 2019.



- Grabowski, D., Enkelmann, E., Ehlers, T.A.: Spatial extend of rapid denudation in the glaciated St. Elias syntaxis region, SE Alaska, *J. Geophys. Res.: Earth Surf.*, 118, 1-18, <https://doi.org/10.1002/jgrf.20136>, 2013.
- 625 Green, P.F.: The relationship between track shortening and fission track age reduction in apatite: combined influences of inherent instability, annealing anisotropy, length bias and system calibration, *Earth Planet. Sci. Lett.*, 89, 335–352, [https://doi.org/10.1016/0012-821X\(88\)90121](https://doi.org/10.1016/0012-821X(88)90121), 1988.
- Guenther, W.R.: Implementation of an alpha damage annealing model for zircon (U-Th)/He thermochronology with comparison to a zircon fission track annealing model, *Geochem. Geophys. Geosys.*, 22, GC008757, <https://doi.org/10.1029/2019GC008757>, 2021.
- 630 Guenther, W.R., Reiners, P.W., Ketcham, R.A., Nasdala, L., and Giester, G.: Helium diffusion in natural zircon: radiation damage, anisotropy, and the interpretation of zircon (U-Th)/He thermochronology, *Am. J. Sci.*, 313, 145–198, <https://doi.org/10.2475/03.2013.01>, 2013.
- Guenther, W.R., Reiners, P.W., DeCelles, P.G., and Kendall, J.: Sevier belt exhumation in central Utah constrained from complex zircon (U-Th)/He data sets: Radiation damage and He inheritance effects on partially reset detrital zircons, *Geol. Soc. Am. Bull.* 127, 323–348, <https://doi.org/10.1130/B31032.1>, 2015.
- 635 Hadlari, T., Tylosky, S.A., Lemieux, Y., Zantvoort, W.G., and Catuneanu, O.: Slope and submarine fan turbidite facies of the Upper Devonian Imperial Formation, Northern Mackenzie Mountains, NWT, *Bull. Can. Energy Geosci.*, 57, 192–208, <https://doi.org/10.2113/gscpgbull.57.2.192>, 2009.
- 640 Härtel, B.: PaRACAS (Partial Reset Analysis for Cooling Ages of Sources) (v1.0), Zenodo [code], <https://doi.org/10.5281/zenodo.18248225>, 2026.
- Härtel, B., and Enkelmann, E.: The daughter-parent plot: a tool for analyzing thermochronological data, *Geochronology*, 6, 429–448, <https://doi.org/10.5194/gchron-6-429-2024>, 2024.
- Härtel, B., Jonckheere, R., Wauschkuhn, B., and Ratschbacher, L.: The closure temperature(s) of zircon Raman dating, *Geochronology*, 3, 259–272, <https://doi.org/10.5194/gchron-3-259-2021>, 2021.
- 645 Härtel, B., Enkelmann, E., and Whelan, E.: Combined zircon U/Pb-(U-Th)/He-Raman dating, *Chem. Geol.*, 123435, <https://doi.org/10.1016/j.chemgeo.2026.123435>, 2026.
- Hasebe, N., Barbarand, J., Jarvis, K., Carter, A., and Hurford, A.J.: Apatite fission-track chronometry using laser ablation icp-ms, *Chem. Geol.*, 207, 135–145, <https://doi.org/10.1016/j.chemgeo.2004.01.007>, 2004.
- 650 Haynes, W.M., Lide, D.R., and Bruno, T.J. (Eds.): *CRC Handbook of Chemistry and Physics*, 95th Edition, CRC Press, Taylor and Francis Group, Boca Raton, Florida, 2666 p., ISBN 978-1482208672, 2014.
- Hurley, P.M., Larsen, E.S., and Gottfried, D.: Comparison of radiogenic helium and lead in zircon, *Geochim. Cosmochim. Acta*, 9, 98–102, [https://doi.org/10.1016/0016-7037\(56\)90060-6](https://doi.org/10.1016/0016-7037(56)90060-6), 1956.
- 655 Issler, D.R., Grist, A.M., and Stasiuk, L.D.: Post-Early Devonian thermal constraints on hydrocarbon source rock maturation in the Keele Tectonic Zone, Tulita area, NWT, Canada, from multi-kinetic apatite fission track thermochronology, vitrinite reflectance and shale compaction, *Bull. Can. Pet. Geol.*, 53, 405–431, <https://doi.org/10.2113/53.4.405>, 2005.
- Jensen, P.K., and Hansen, K.: Deconvolution of fission-track length distributions and its application to dating and separating pre- and post-depositional components, *Geochronology*, 3, 561–575, <https://doi.org/10.5194/gchron-3-561-2021>, 2021.
- 660 Jensen, P.K., Hansen, K., and Kunzendorf, H.: A numerical model for the thermal history of rocks based on confined horizontal fission tracks, *Nucl. Tracks Radiat. Meas.*, 20, 349–359, [https://doi.org/10.1016/1359-0189\(92\)90064-3](https://doi.org/10.1016/1359-0189(92)90064-3), 1992.
- Jess, S., Enkelmann, E., and Matthews, W.: The effect of sediment storage in glaciated catchments on multiminerall detrital geochronology: deciphering conflicting zircon and apatite U-Pb dates, *J. Geophys. Res. Earth Surf.*, 128, e2022JF006738, <https://doi.org/10.1029/2022JF006738>, 2023.
- 665 Jost, W.: *Diffusion in solids, liquids and gases*, Academic Press Inc., New York, 558 p., ISBN 978-0123907509, 1952.
- Keil, R., Pahl, M., and Bertagnolli, E.: Thermal history and length distribution of fission tracks: Part II, *Nucl. Tracks Radiat. Meas.*, 13, 25–33, [https://doi.org/10.1016/1359-0189\(87\)90004-5](https://doi.org/10.1016/1359-0189(87)90004-5), 1987.
- 670 Ketcham, R.A.: Forward and inverse modeling of low-temperature thermochronometry data, *Rev. Mineral. Geochem.*, 58, 275–314, <https://doi.org/10.2138/rmg.2005.58.11>, 2005.



- Ketcham, R.A.: Thermal history inversion from thermochronometric data and complementary information: New methods and recommended practices, *Chem. Geol.*, 653, 122042, <https://doi.org/10.1016/j.chemgeo.2024.122042>, 2024.
- 675 Ketcham, R.A., Gautheron, C., and Tassan-Got, L.: Accounting for long alpha-particle stopping distances in (U-Th-Sm)/He geochronology: refinement of the baseline case, *Geochim. Cosmochim. Acta*, 75, 7779–7791, <https://doi.org/10.1016/j.gca.2011.10.011>, 2011.
- Lemieux, Y., Hadlari, T., and Simonetti, A.: Detrital zircon geochronology and provenance of Devonian–Mississippian strata in the northern Canadian Cordilleran miogeocline, *Can. J. Earth Sci.*, 48, 515–541, <https://doi.org/10.1139/E10-056>, 2011.
- 680 Lovera, O.M., Richter, F.M., and Harrison, T.M.: The $^{40}\text{Ar}/^{39}\text{Ar}$ thermochronometry for slowly cooled samples having a distribution of diffusion domain sizes, *J. Geophys. Res.*, 94, 17917–17935, <https://doi.org/10.1029/JB094iB12p17917>, 1989.
- Malusà, M.G., and Fitzgerald, P.G.: The geologic interpretation of the detrital thermochronology record within a stratigraphic framework, with examples from the European Alps, Taiwan and the Himalayas, *Earth-Sci. Rev.*, 201, 103074, <https://doi.org/10.1016/j.earscirev.2019.103074>, 2020.
- 685 Malusà, M.G., Anfinson, O.A., and Stockli, D.F.: (Mis)identification of magmatic and exhumation ages by detrital zircon U-Pb and He double dating: a case study from the Bergell-Gonfolite system (European Alps), *Chem. Geol.*, 606, 120970, <https://doi.org/10.1016/j.chemgeo.2022.120970>, 2022.
- 690 McKay, R., Enkelmann, E., Hadlari, T., Matthews, W., and Mouthereau, F.: Cenozoic exhumation history of the eastern margin of the Northern Canadian Cordillera, *Tectonics*, 40, e2020TC006582, <https://doi.org/10.1029/2020TC006582>, 2021.
- Meesters, A.G.C.A., and Dunai, T.J.: Solving the production–diffusion equation for finite diffusion domains of various shapes Part II. Application to cases with α -ejection and nonhomogeneous distribution of the source, *Chem. Geol.*, 186, 57–73, [https://doi.org/10.1016/S0009-2541\(01\)00423-5](https://doi.org/10.1016/S0009-2541(01)00423-5), 2002.
- 695 Morton, A.C.: The provenance and diagenesis of Palaeogene sandstones of southeast England as indicated by heavy mineral analysis. *Proc. Geol. Assoc.*, 93, 263–274, [https://doi.org/10.1016/S0016-7878\(82\)80003-5](https://doi.org/10.1016/S0016-7878(82)80003-5), 1982.
- O’Sullivan, G., Chew, D., Kenny, G., Henrichs, I., and Mulligan, D.: The trace element composition of apatite and its application to detrital provenance, *Earth-Sci. Rev.*, 201, 103044, <https://doi.org/10.1016/j.earscirev.2019.103044>, 2020.
- 700 Powell, J.W., and Schneider, D.A.: Preliminary results of $^{40}\text{Ar}/^{39}\text{Ar}$ geochronology from the eastern Mackenzie Mountains and Mackenzie Plain, Northwest Territories, Geological Survey of Canada Current Research, 2013-8, 20p, 2013.
- Powell, J.W., Schneider, D., Stockli, D., and Fallas, K.: Zircon (U-Th)/He thermochronology of Neoproterozoic strata from the Mackenzie Mountains, Canada: Implications for the Phanerozoic exhumation and deformation history of the northern Canadian Cordillera, *Tectonics*, 35, 663–689, <https://doi.org/10.1002/2015TC003989>, 2016.
- 705 Powell, J.W., Issler, D.R., Schneider, D.A., Fallas, K.M., and Stockli, D.F.: Thermal history of the Mackenzie Plain, Northwest Territories, Canada: Insights from low-temperature thermochronology of the Devonian Imperial Formation, *Geol. Soc. Am. Bull.*, 132, 767–783, <https://doi.org/10.1130/B35089.1>, 2020.
- Rahl, J.M., Reiners, P.W., Campbell, I.H., Nicolescu, S. and Allen, C.M.: Combined single-grain (U-Th)/He and U/Pb dating of detrital zircons from the Navajo Sandstone, Utah, *Geology*, 31, 761–764, <https://doi.org/10.1130/G19653.1>, 2003.
- 710 Rahl, J.M., Haines, S.H., and van der Pluijm, B.A.: Links between orogenic wedge deformation and erosional exhumation: Evidence from illite age analysis of fault rock and detrital thermochronology of syn-tectonic conglomerates in the Spanish Pyrenees, *Earth Planet. Sci. Lett.*, 307, 180–190, <https://doi.org/10.1016/j.epsl.2011.04.036>, 2011.
- 715 Reiners, P.W., and Farley, K.A.: Influence of crystal size on apatite (U-Th)/He thermochronology: an example from the Bighorn Mountains, Wyoming, *Earth Planet. Sci. Lett.*, 188, 413–420, [https://doi.org/10.1016/S0012-821X\(01\)00341-7](https://doi.org/10.1016/S0012-821X(01)00341-7), 2001.
- Reiners, P. W., Spell, T. L., Nicolescu, S., and Zanetti, K.A.: Zircon (U-Th)/He thermochronometry: He diffusion and comparisons with $^{40}\text{Ar}/^{39}\text{Ar}$ dating, *Geochim. Cosmochim. Acta*, 68, 1857–1887, <https://doi.org/10.1016/j.gca.2003.10.021>, 2004.



- 720 Reiners, P.W., Campbell, I.H., Nicolescu, S., Allen, C.M., Hourigan, J.K., Garver, J.I., Mattinson, J.M., and Cowan, D.S.: (U-Th)/(He-Pb) double dating of detrital zircons, *Am. J. Sci.*, 305, 259–311, <https://doi.org/10.2475/ajs.305.4.259>, 2005.
- Rufino, M., Lixandrão-Filho, A.L., and Guedes, S.: A reappraisal of the principle of equivalent time based on physicochemical methods, *Chem. Geol.*, 627, 121459, <https://doi.org/10.1016/j.chemgeo.2023.121459>, 2023.
- 725 Satopää, V., Albrecht, J., Irwin, D., and Raghavan, B.: Finding a “kneedle” in a haystack: Detecting knee points in system behavior, in: *Proceedings of the 31st International Conference on Distributed Computing Systems*, Minneapolis, Minnesota, June 2011, Workshops, 166-171, 2011.
- Spalding, J., Powell, J.W., Schneider, D.A., and Fallas, K.M.: Thermal history of the Peel Plateau, northern Canadian Cordillera, resolved through multikinetic apatite fission-track dating, *Mar. Pet. Geol.*, 155, 106358, <https://doi.org/10.1016/j.marpetgeo.2023.106358>, 2023.
- 730 Stevens Goddard, A.L., Black, S.R., Baggot, E.A., Anderson, Z.W., Leary, R.J., Thurston, O.G., and Yonkee, W.A.: Detrital thermochronology histories preserved in Paleogene strata of Utah (USA) provide distant records of Paleozoic Alleghanian orogenesis and sediment dispersal, *Geology*, 53, 217–221, <https://doi.org/10.1130/G52736.1>, 2024.
- 735 Sundell, K.E., and Saylor, J.E.: Two-dimensional quantitative comparison of density distributions in detrital geochronology and geochemistry, *Geochem. Geophys. Geosys.* 22, e2020GC009559, <https://doi.org/10.1029/2020GC009559>, 2021.
- Thomson, D., Schröder-Adams, C.J., Hadlari, T., Dix, G., and Davis, W.J.: Albian to Turonian stratigraphy and paleoenvironmental history of the northern Western Interior Sea in the Peel Plateau Region, Northwest Territories, Canada, *Palaeogeography, Palaeoclimatology, Palaeoecology*, v. 302, p. 270-300, <https://doi.org/10.1016/j.palaeo.2011.01.017>, 2011.
- 740 Tripathy-Lang, A., Hodges, K.V., Monteleone, B.D., and van Soest, M.C.: Laser (U-Th)/He thermochronology of detrital zircons as a tool for studying surface processes in modern catchments, *J. Geophys. Res. Earth Surf.*, 118, 1333–1341, <https://doi.org/10.1002/jgrf.20091>, 2013.
- 745 Vermeesch, P., Sherlock, S.C., Roberts, N.M.W., and Carter, A.: A simple method for in-situ U-Th-He dating, *Geochim. Cosmochim. Acta*, 79, 140–147, <https://doi.org/10.1016/j.gca.2011.11.042>, 2012.
- Yonkee, W.A., Eleogram, B., Wells, M.L., Stockli, D.F., Kelley, S., and Barber, D.E.: Fault slip and exhumation history of the Willard thrust sheet, Sevier fold-and-thrust belt, Utah: relations to wedge propagation, hinterland uplift, and foreland basin sedimentation, *Tectonics*, 38, 2850–2893, <https://doi.org/10.1029/2018TC005444>, 2019.
- 750 Zawacki, E.E., van Soest, M.C., Hodges, K.V., Scott, J.J., Barboni, M., Strecker, M.R., Feibel, C.S., Campisano, C.J., and Arrowsmith, J.R.: Sediment provenance and silicic volcano-tectonic revolution of the northern East-African Rift System from U/Pb and (U-Th)/He laser ablation double dating of detrital zircons, *Earth Planet. Sci. Lett.*, 580, 117375, <https://doi.org/10.1016/j.epsl.2022.117375>, 2024.
- Ziegler, J.F.: SRIM – The Stopping and Range of Ions in Matter, <http://www.srim.org>, 2013.